Programmatic perspectives with technical examples for THz materials characterization

Walter Buchwald
Air Force Research Laboratory, Sensors Directorate, Hanscom AFB, MA

ABSTRACT

THz technology has a rich history of use in the field of interstellar molecule identification where a variety of molecule specific vibrational and rotational spectroscopic signatures exist and has been aggressively investigated for use in advanced radar applications because of the immediate improvement in object resolution obtained at higher frequencies. Traditionally, high power THz systems have relied upon millimeter wave sources and frequency multiplication techniques to achieve acceptable output power levels, while lower power, table top spectroscopic systems, have relied on broadband incoherent light sources. With the advent of high power lasers, advances in non-linear optics, and new material systems, a number of promising techniques for the generation, detection and manipulation of THz radiation are currently under development and are considered the enabling technologies behind a variety of advanced THz applications.

This work presents a programmatic overview of current trends in THz technology of interest to a variety of government organizations. It focuses on those techniques currently under investigation for the generation and detection of THz fields motivated, for example, by such diverse applications as metamaterial spectroscopy, TH imaging, long standoff chem/bio detection and THz communications. Examples of these new techniques will be presented which in turn will motivate the need for the characterization of application specific active and passive THz components.

Keywords: THz, comb-FTIR, metamaterials, plasmonics, quantum optics

1. INTRODUCTION

Recent advances in such diverse fields as non-linear optics, metamaterials, high temperature superconductors, plasmonics, nano-membranes and optical communications have motivated a number of research efforts intent on exploring the usefulness of THz frequencies beyond those areas traditionally pursued [1-6]. The classical THz applications of astronomy, space science [7], and THz RADAR [8], which exploits the improved spatial resolution obtained at shorter wavelengths when compared to mm-wave systems, are not only benefiting from these research areas but entirely new applications, such as THz radio for ultra-secure satellite to satellite communications and the encoding of information onto optical carriers for low loss THz data-links are being envisioned [9,10]. In other areas, THz sensor arrays, with the capability of imaging through dust laden environments as well as THz based remote sensing, which relies on laser induced plasma fluorescence to remotely convey THz spectroscopic information through inherently lossy environments, are expected to play key roles in homeland security and remote environmental monitoring [11-14]. To fully implement these advanced concepts the development of both discreet and integrated components will be required, which, in-turn, will require a detailed understanding of the underlying material response at THz frequencies as well as a greater spectroscopic signature catalogue then is currently available.

Beyond the system level, material investigations at THz frequencies are expected to make an impact on such fields as metamaterials and quantum optics [15-17]. Experimental metameterials research requires the fabrication of structures intent on producing a system response unavailable in the materials "natural" state, through the control of material permittivity, permeability or both. This is typically accomplished through the fabrication of metallic structures of an appropriate geometry with dimensions less than the wavelength of the exciting radiation. The theoretical means to predict such system response through transformational optics currently out-paces the ability to fabricate and measure

Micro- and Nanotechnology Sensors, Systems, and Applications III, edited by
Thomas George, M. Saif Islam, Achyut K. Dutta, Proc. of SPIE Vol. 8031, 80310F
 · doi: 10.1117/12.884599

these structures over all wavelengths of interest. By operating at longer, THz wavelengths, fabrication constraints are relaxed and experimental results can be obtained in order to confirm theory. This same argument of relaxed fabrication requirements at longer wavelengths is also used to motivate quantum optics research. At THz frequencies, both dielectric and metallic waveguide loss is minimized and the fabrication of the small volume cavities, needed to form the coupled cavity quantum electrodynamic system required for the exploration of the light/matter interactions at the quantum limit, becomes more tenable.

Finally, all of the above mentioned applications will require advances in spectroscopic techniques for the characterization of not only the underlying material but also for the characterization of improved THz light sources, detectors and components. For example, it is envisioned that comb-FTIR, which relies on the beating of two slightly detuned mode-locked femto-second lasers to produce an interferogram via multi-frquency heterodyne detection, can be extended to THz frequencies [18,19]. The exploitation of resonant plasmon modes in the two dimensional electron gas of a high electron mobility transistor has been proposed as a means to tunably detect THz radiation for "spectrometer-on-a chip" applications [20]. Tunable Fabry-Perot cavities, fabricated from nanomembrane based, low loss, Fano-reflectors, could be used not only as long wave spectrometers in the field of astrophysics, but, with the incorporation of a quantum cascade laser as a gain medium, for use as a compact, man portable, high precision chemical sensor for homeland security applications [21,22].

This paper presents a number of these THz critical programs in more detail and outlines the material and component characterization requirements of each. It is hoped that by presenting these primarily defense related programs and needs to a broader technical community a more widespread interest in THz technology will result leading to increased awareness and further technical advancements.

2. THz APPLICATIONS

2.1 Metamaterials

The field of metamaterials has received much interest of late and experimental verification of theory and numeric solutions, offer great opportunities for THz material characterization [23-29]. Briefly, if a material exhibits a strong response to electromagnetic fields, but is of dimensions smaller than the wavelength of the exciting radiation, a carefully constructed aggregate of the material can be treated as a homogenous medium described by an effective permittivity and effective permeability with values that differ greatly from the original material constants. To illustrate the power of this effect, consider the classical wave equation obtained from Maxwell's Equations, namely

$$\frac{\partial^2 E(x,t)}{\partial x^2} = \varepsilon\mu \ \frac{\partial^2 E(x,t)}{\partial t^2} \tag{1}$$

where, ε is the electric permittivity, μ is the magnetic permeability and $E(x,t)$ is the electric field. In general, oscillatory solutions exist only if the product, $\varepsilon\mu$, is positive. This is readily apparent for metals, which, due to strong interactions between free electrons, become opaque to frequencies of radiation which fall below the so called plasma frequency, ω_p , or, alternatively, at those frequencies where the permittivity becomes less than zero. However, it has been shown, that a carefully constructed matrix of cut wires, with cross sectional diameters much less than the wavelength of radiation and properly spaced, does not simply become transparent, but can exhibit a response equivalent to a bulk material with a plasma frequency many orders of magnitude less than the metal used in the cut wires themselves. This response, caused by field induced currents and mutual inductance, is the reason metal wires can be considered one of the fundamental building blocks of metamaterials as they alter the electrical permittivity of space in a manner not attainable using bulk materials alone. It can be shown that the effective permittivity of a cut wire medium can be described by

$$\varepsilon_{eff}(\omega) = 1 - \frac{\omega_{ep}^2 - \omega_o^2}{\omega^2 - \omega_o^2 + i\omega\omega_\tau} \tag{2}$$

where ω_{ep}, and ω_o are the new, effective plasma frequency and resonance frequency, both of which are determined by geometry as opposed to charge density and effective mass. ω_τ is the relaxation frequency of traditional Drude theory. In

fact, equation (2) above exactly reproduces the permittivity of Drude theory if ω_{ep} is replaced by the plasma frequency and ω_o is set to zero. It is clear from this equation that a region of negative permittivity exists when $\omega_o < \omega < \omega_{ep}$ leading to no oscillatory solutions for Equation (1) above in this so called "stop-band" region.

Although Equation (2) represents a means to control a materials permittivity and in-turn a loss of transparency at frequencies not normally attainable, negative permittivity materials in general, i.e. metals, are commonplace. Negative permeability materials, on the other hand, are not so abundant in nature and if available, would give even more control over propogating electromagnetic fields. In 1999 Pendry et.al.[24] demonstrated theoretically that such a negative permeability system could be developed through the use of induced currents circulating in closed loops acting as inductors. Introducing gaps in these loops effectively added a capacitive element to the system forming a resonant LC circuit, with resonant features completely controlled by material geometry. This so called split ring resonator, SRR, is thus considered the second "building-block" of metamaterials and is shown to have an effective permeability given by

$$\mu_{eff}(\omega) = 1 - \frac{F\,\omega^2}{\omega^2 - \omega_0^2 + i\omega\omega_\tau} \tag{3}$$

where F is the fractional volume of the unit cell occupied by the SRR and all other symbols as previously defined. Based on Equations (2) and (3), a means is at hand, at least theoretically, to have unprecedented control over propogating electromagnetic fields by introducing material of dimensions must smaller than the wavelength of the incident radiation, but having the ability to strongly interact with those same fields, which, in turn introduces a material response unattainable by the bulk form of the mediums constituents. In fact, by considering the typical definition of a materials index of refraction, n, namely

$$n = \sqrt{\varepsilon\mu} \tag{4}$$

and realizing that both the permittivity and permeability are in general complex values such that $\varepsilon = \exp(i\pi)$ and $\mu = \exp(i\pi)$ lead to negative values for both the permittivity and permeability, a proper treatment of Equation (4) leads to

$$n = \sqrt{\exp(i\pi)\exp(i\pi)} = \exp\left(i\frac{\pi}{2}\right)\exp\left(i\frac{\pi}{2}\right) = \exp(i\pi) = -1 \tag{5}$$

This so called "negative index" was hypothesized by Victor Veselago in 1967 and forms the basis of those metamaterials now called "left handed materials" which have no naturally occurring counterparts [30].

In general, there are very few geometries which lend themselves to analytic solutions for the effective permittivity and

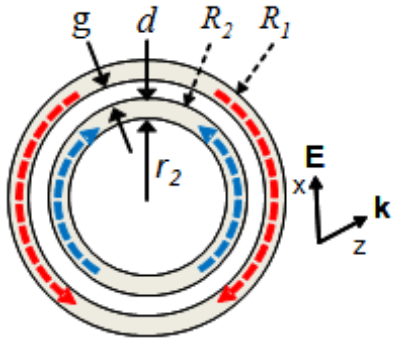

Figure 1: Dual concentric ring metamaterials structure. FEM simulations were performed with R_1=30μm, R_2=24μm, g=3μm, the thickness of the Au metal ring is 400nm. The direction of the incident radiation and the electric field polarization is also shown. In the simulation, the material surrounding the ring has an index of refraction of 1 unless otherwise indicated in the text.

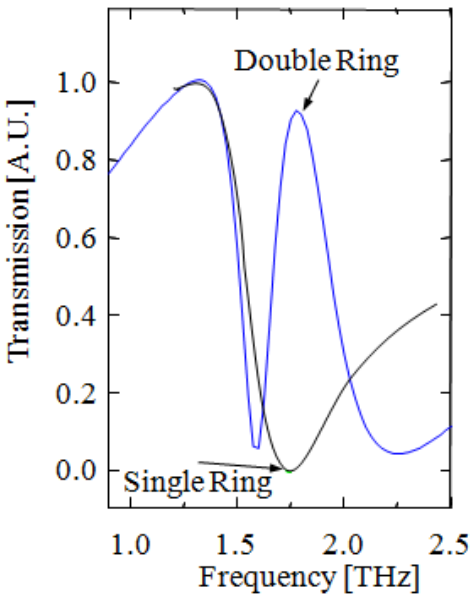

Figure 2: Simulated power flow through the single and double concentric ring structure.

permeability of metamaterials. Because of this, there is a heavy reliance on numeric solutions using finite element methods, FEM's. For example, Figure 1 shows a multiple concentric ring structure with dimensions as indicated [16].

Power flow through this structure as a function of incident frequency, with and without the central ring, is shown in Figure 2. Simulations clearly predict a reduction in transmitted power at roughly 1.75THz for the single ring structure which is canceled out by the addition of the second ring causing a "transparency window". Although not shown in this figure, the addition of more inner rings, adds additional transparency windows at increasing frequencies while having little effect on the original response of the outermost rings. The cause of this response can best be visualized by considering Figure 3, which shows electromagnetic power flow as well as ring current at three different excitation frequencies for a quad concentric ring structure. At 1.6 THz and 2.0THz, large field induced ring currents dominate while these currents are dramatically reduced in the transparency window at 1.75THz.

For this concentric ring structure, it was found that the resonance position, f_r, of the transparency window can be obtained through the following simple relation,

$$f_r = \frac{c}{2\,\pi\,R_{12}} \tag{6}$$

where c is the speed of light and R_{12} is the average radius of any two adjacent rings, which, for the values given in Figure 1, leads to a resonance frequency of 1.76THz in good agreement with the simulated results. This suggests a very simple means to tailor the systems response to any desired frequency, however, if one considers the situation as shown in Figure 4, where the index of refraction is changed to reflect the rings patterned on a substrate with a refractive index greater than one, dramatic shifts in resonance frequency are seen which are difficult to account for by any simple modification to Equation (6). Metamaterial characterization is therefore required not only to validate theory, but also to establish

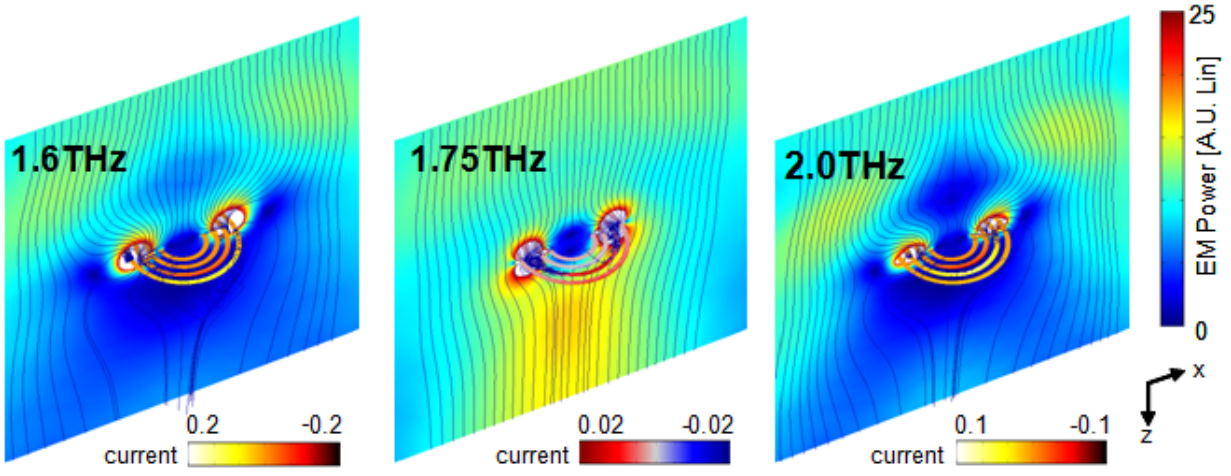

Figure 3: Simulated power flow and induced currents in a quad concentric ring structure. Inductive coupling between outermost rings at 1.75 THz is seen to produce a "transparency window" between transmission minimum at 1.6THz and 2.0THz. Note the change in scale for ring current magnitude for each frequency.

relationships between material properties which might not scale linearly with characteristic lengths.

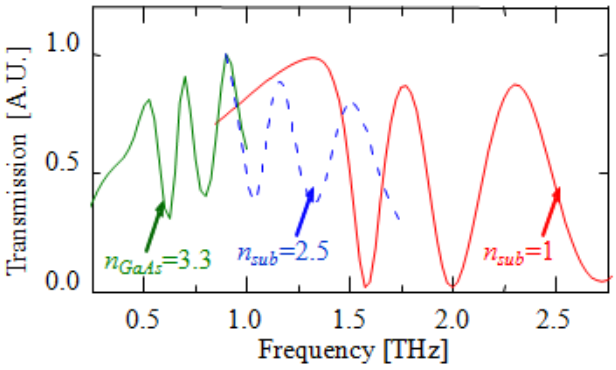

Figure 4: Simulated transmission through multi-concentric ring metamaterial as a function of substrate refractive index.

At this point, spectroscopic investigations concerning metamaterials, due to their use in producing an electromagnetic response not attainable by materials in their bulk state, seems warranted in order to both confirm theory as well as to establish practical relationships between the basic metamaterial building blocks and those materials needed to support them. The motivation for THz spectroscopy specifically, becomes apparent when one considers the relative size requirements of the metamaterial components and the means presently available to fabricate those components as well as the losses that are introduced as the excitation frequency increases. Historically, metamaterial investigations were performed at millimeter wavelengths or GHz frequencies. This required characteristic lengths to be on the order of tenths of millimeters or hundred of microns and the losses at these frequencies are low. At these frequencies the interest lies, primarily, in their use for advanced antenna applications, radar "cloaking" and as a means to investigate metamaterial concepts. Fabrication of such structures at these wavelengths can be undertaken using bulk micro-machining technology. Once the most fundamental metamaterials concepts were verified, however, interest turned to applications at shorter wavelengths where photonic metamaterials were envisioned for applications such as visible cloaking and flat lenses. In general, as the frequency of excitation increases, the characteristic lengths get shorter and transmission losses are no longer negligible. In fact, for a metamaterial structure operating at 100THz, or over wavelengths from roughly 1μm to 4μm, the lengths associated with a SRR, fabricated on low dielectric constant material, fall between 70nm to 320nm [31]. The fabrication of such structures is now far more complex requiring advanced e-beam lithographic techniques, which can produce arrays of structures over only a relatively small area, or through the use of reduction stepper technology, which brings the cost of fabrication far beyond that available to most research institutions. The problem is further compounded when propagation loss is considered. For the case of a Au structure, and assuming all loss is related to bound surface modes, or surface plasmon polaritons, (SPP's), the SPP propagation loss can be calculated via [32]

$$Loss(\omega) = 2\, Im(k_{spp}) \tag{7}$$

Where k_{spp} is the surface plasmon polariton wavevector obtained from the SPP dispersion relation

$$k_{spp} = \frac{\omega}{c}\sqrt{\frac{\varepsilon(\omega)\varepsilon_d}{\varepsilon_d+\varepsilon(\omega)}} \tag{8}$$

ω is the excitation frequency and ε_d is the dielectric permittivity. The frequency dependant permittivity of the conductor is given by standard Drude theory as

$$\varepsilon(\omega) = \varepsilon_\infty\left[1 - \frac{\omega_p^2}{\omega\,(\omega+i\omega_\tau)}\right] \tag{9}$$

with ω_p being the plasma frequency, ω_τ the relaxation frequency and ε_∞ is the conductor permittivity at infinite frequency, assumed to be unity for Au . For Au, with values for a plasma frequency and relaxation frequency of $1.4\text{x}10^{16}$ rad/sec and $4.0\text{x}10^{13}$ rad/sec respectively, it is seen that for every order of magnitude increase in excitation frequency the SPP related loss increases by two orders of magnitude. Thus, loss, which can be neglected at GHz frequencies increases by 10 orders of magnitude when the metamaterial structures are scaled to 100THz and now takes on a prominent role in system response. Metamaterial characterization at THz frequencies therefore, represents a tradeoff between loss and fabrication complexity. By focusing on those structures that are on the micron scale, standard contact lithography can be

used to generate relatively complex patterns over large areas. Interactions between these structures are more easily investigated and scaling effects associated with both the structures themselves and the dielectrics supporting them can be investigated.

2.2 Active Plasmonics

Plasmonics exploits the strong interactions and highly non-linear dispersion relation associated with Equation (8) above, along with the frequency dependant permittivity of Equation (9) [33, 34]. Active plasmonics exploits the use of charge control to preferentially excite a desired plasmon mode. Plasmons in general can be understood by assuming $\omega_{p>>}\omega_{\tau}$, which is true for most metals, which leads to solutions to Equation (8) as shown in Figure 5. In this figure, there are two branches associated with the dispersion relation; one branch which lies above the light line and one that lies below the light line. At frequencies above the plasma frequency the conductor becomes essentially transparent. Below the plasma frequency and the so called surface plasmon frequency, ω_{sp}, given by

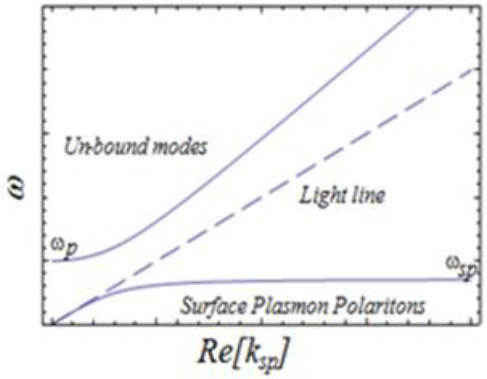

Figure 5: Real part of solution to Equation (8) in text showing both unbound and surface plasmon polariton branches

$$\omega_{sp} = \frac{\omega_p}{\sqrt{1+\varepsilon_d}} \qquad (10)$$

a propagating electromagnetic mode exists which is bound to the interface between the metal and the dielectric, this is the so-called SPP mode referred to above. In the region $\omega_p > \omega > \omega_{sp}$ the material is not transparent but also will not support a bound mode. A more complete analytical investigation reveals plasmons modes to be composed of three, transverse wave vectors, one, k_{sp} mentioned above, which lies in the plane of the interface and propagates in the direction of the SPP, The other two wave vectors point in directions normal to the interface, with k_d pointing into the dielectric and k_c pointing into the conductor, all of which, in general, are complex valued. The complete description of a SPP is contained in the relative magnitudes of the real and imaginary parts of these wave vectors, two of which are shown in Figure 6, (a) and (b) below. Here we see from the in-plane wavevector of Figure 6 (a), k_{sp}, that at frequencies $\omega_{sp} > \omega > \omega_p$, $\mathrm{Re}[k_{sp}] >> \mathrm{Im}[k_{sp}]$ suggesting an under-damped oscillatory solution. At frequencies such that $\omega_p > \omega > \omega_{sp}$ $\mathrm{Im}[k_{sp}] >> \mathrm{Re}[k_{sp}]$ indicating strong absorption. From the transverse wave vector of Figure 6 (b), k_d, we see when $\omega > \omega_{sp}$, $\mathrm{Re}[k_d] >> \mathrm{Im}[k_d]$ and when $\omega < \omega_{sp}$ $\mathrm{Im}[k_d] >> \mathrm{Re}[k_d]$. Taken together, these wave vectors produce a propogating electromagnetic wave when $\omega > \omega_p$ in the dielectric and a bound, evanescent wave at the interface when $\omega < \omega_{sp}$ which propagates in the direction of k_{sp} and decays exponentially in a direction normal to the surface. An analysis of Equation (9) above also reveals that when

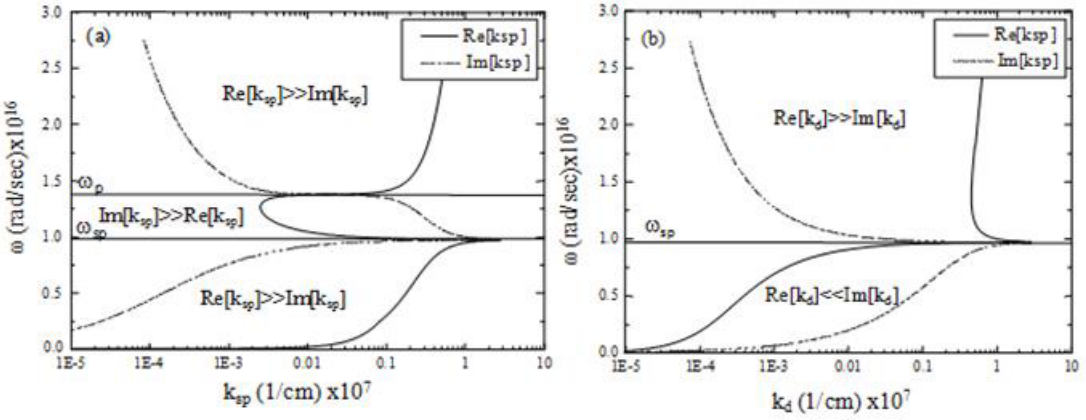

Figure 6: (a) SPP in-plane wave vector pointing in direction of propagation and (b) SPP transverse wave vector pointing into dielectric.

$\omega<\omega_p$, the relative permittivity of the metal becomes negative, consistent with the previous assertion of no oscillatory solution to Maxwells's equation's when either the permittivity, or the permeability, but not both, becomes negative. Because of the highly non-linear nature of the SPP branch, the use of SPP's allows optical field focusing beyond the traditional diffraction limit as well as for use in low loss wave guiding applications [35,36]. It is pointed out however, that from a practical point of view, a low loss SPP mode will fall closer to the light line of Figure (5) and as such will have poor mode confinement while a tightly bound mode will have far greater loss. This tradeoff between loss and mode confinement has motivated research into the use of other material systems besides noble metals as SPP hosts particularly at the longer wavelengths [32].

Referring to Figure 5, because SPP modes always fall below the light line the wave vector k_{sp} will always be greater than the wave vector used to excite the mode, k_i. This implies a lack of sufficient incident momentum to directly excite a plasmon mode from an incident optical field. To alleviate this problem, numerous methods have been developed to add momentum to the incident excitation, one of these being the use of a diffraction grating [37-39]. A diffraction grating will add momentum in the direction of SPP prorogation in units of

$$K_G = \frac{2\pi m}{p} \tag{11}$$

where m is an integer, the diffraction order, and p is the period of the grating. When the incident momentum is sufficient, incident radiation will no longer be supplied to any allowed diffraction order, instead, a surface plasmon will result. This is observed as a reduction in intensity of light associated with the zeroth order reflection from a diffraction grating and is the source of the so-called, "resonant Woods anomalies" first observed in 1902 by R. Wood [40].

In general, a conductor's plasmon frequency is related to the response of electrons to the driving field relative to an ionic background and the relaxation frequency is related to the electron collision rate. ω_p is defined as

$$\omega_p \equiv \sqrt{\frac{Nq^2}{\varepsilon_o m_o}} \tag{12}$$

and

$$\omega_\tau = \frac{1}{\tau} \tag{13}$$

Where is N is the electron concentration, q is the electron charge, ε_o and m_o are the permittivity of free space and electron rest mass respectively and τ is the electron momentum relaxation time. Because of the dependence of plasmon frequency on electron concentration and because the plasmon frequency plays a prominent role in the SPP dispersion relation, any material system that offers control of charge concentration also offers control over the SPP dispersion relation and in-turn control of the allowed plasmon mode. This control over the allowed plasmon mode is exploited in the field of active plasmonics.

It is well known that an externally applied bias can control the sheet charge concentration associated with a high electron mobility transistor or HEMT. This has motivated the use of HEMT's in the field of active plasmonics [20,41,42]. The epitaxial layer structure of a generic InAlAs/InGaAs HEMT is shown in Figure 7 (a). Due to the conduction band offsets associated with InAlAs and InGaAs, a triangular shaped well is formed at the InAlAs/InGaAs interface which, if properly designed, can fall below the quasi-electron Fermi level for electrons, E_f, as shown in Figure 7 (b). By falling below the Fermi level, a large concentration of highly mobile charge, the so called "two dimensional electron gas" or 2deg, forms at the interface as shown in Figure 7 (c). If an external reverse bias is applied to the HEMT's gate, the interfacial well is shifted upwards relative to the Fermi level causing a rapid reduction in charge concentration. It has been shown, that plasmon generation in a 2deg leads to changes in device current and, due to the typical concentration of electrons in a 2deg, this class of device operates in the long wavelength regime, offering opportunities for THz material and device characterization [42]. Such a class of device can be considered a frequency agile detector and has been proposed for use in spectrometer-on-a-chip applications, in chemical/biological sensing scenarios and in THz imaging applications where the possibility of fabrication into an array format could be exploited for homeland security and imaging through dust laden environments.

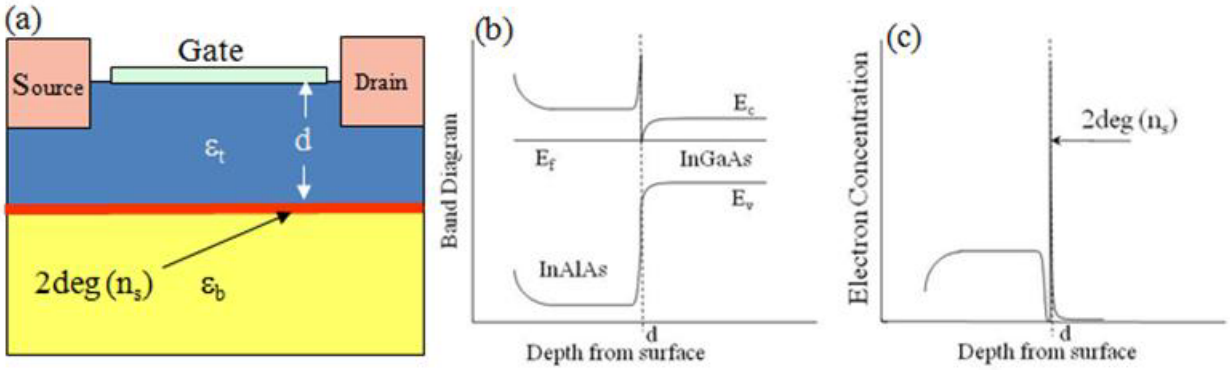

Figure 7: (a) Generic HEMT epilayers (b) generic HEMT band diagram (c) HEMT electron concentration. Band bending causes the Fermi level ito the conduction band at the hetero-interface causing the formation of a two dimensional electron gas.

In a conductor, an external excitation displaces the mobile electrons with a restoring force supplied by the lattice of background ions. This induced charge oscillation, in essence is the SPP. In a 2deg, the restoring force associated with the electron displacement is caused by the potential well of the semiconductor itself. Because of this, the dispersion relation for SPP excitation in a 2deg is slightly different than that given in Equation (8) and takes the form

$$\omega(d) = \sqrt{\frac{n_s q^2 K_G}{m^* \varepsilon_o (\varepsilon_b + \varepsilon_t \, Coth(K_G d))}} \tag{14}$$

where m^* is the effective mass of carriers in the 2deg, ε_b, ε_t and d are the relative permittivity's of the material on either side of the 2deg and the distance of the 2deg from the surface of the wafer as shown in Figure 7 (a) respectively. The sheet charge of the 2deg, n_s, can be controlled by a bias applied to the gate of the 2deg which in turn allows for control of the allowed plasmon mode.

Figure 8 (a) shows a scanning electron micrograph of a plasmon mediated detector fabricated using standard semiconductor processing techniques. The inset to Figure 8 shows the gate which was fabricated into a grating using e-beam lithography to allow the gate to serve the dual purpose of 2deg sheet charge control and plasmon coupler. Figure 8 (b) plots the dispersion relation of Equation (14) as a function of sheet charge density and grating period. Here is seen that for a reasonable sheet charge of $3x10^{12}$ cm^{-2} and a sub-micron grating period of 0.5μm, an excitation wavelength of

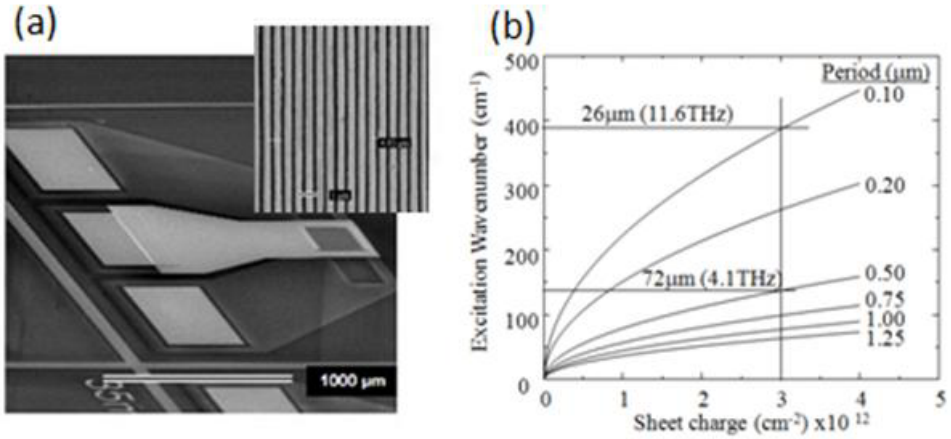

Figure 8: (a) SEM micrograph of the HEMT based plasmon detector. Inset shows submicron gate/grating used as plasmon coupler. (b) Excitation wavenumber as a function of sheet charge density and grating period.

72μm (4.1THz) would be required to achieve momentum matching and plasmon excitation. Increasing the grating period to 1.25μm, within the range of contact lithography as opposed to e-beam lithography, pushes the SPP excitation wavelength to 200μm (1.5THz).

Figure 9 (a) shows experimentally results of FTIR transmission measurements through this device using a Si bolometer detector. The oscillations observed are attributed to Fabry-Perot effects associated with this sample. At wavenumbers indicated by the triangles in Figure 9 (a) a reduction in the Fabry-Perot oscillations are seen. This is attributed to an increase in loss through the sample as the incident field couples to an allowed plasmon mode. As shown in the figure, as the reverse bias on the gate is increased, these plasmon excitations are seen to shift to lower wavenumbers, consistent with Equation (14) and a bias controlled reduction in the sheet charge density. Figure 10 (b) plots plasmon excitation wavenumber as a function of sheet charge density along with the experimentally determined plasmon resonances. Here is seen only a marginal fit between experiment and theory questioning the validity of Equation (14) above.

In order to determine the cause of the discrepancy between experiment and theory, simulations were performed using a commercial finite element solver, Silvaco BALZE, to determine the actual sheet charge concentration based on the epilayer structure of the measured device. The epilayer structure, shown in Figure 10 (a), was simulated and both the band structure and the charge density calculated and plotted in Figure 10 (b). Figure 10 (a) represents the epilayer structure only under the gate region. A highly doped InGaAs cap layer, located under the source and drain, used to facilitate ohmic contact formation, is not shown, as this layer is removed with selective etching prior to the gate formation. In Figure 10 (b) is seen, not only the two deg sheet charge concentration roughly 445nm below the gate contact, but another potential well with a substantial amount of charge located 400nm below the surface. This apparent incomplete transfer of charge from the shallow donors into the 2deg is believed to be the cause of the discrepancy between theory and experiment and has motivated a new dispersion relation which takes the form [43]

$$\left(\varepsilon_b Sinh(K_G b) + \varepsilon_t Cosh(K_G b)\left(\omega^2 - \omega_p^2(b)\right) + \frac{i\sigma_o K_G Sinh(K_G(b-a)}{\varepsilon_o \varepsilon_t \omega}\left(\varepsilon_b Sinh(K_G a) + \varepsilon_t Cosh(K_G a)\right)\left(\omega^2 - \omega_p^2(a)\right) = 0 \right. \quad (15)$$

where ω_p is obtained from equation (14), σ_o is the conductivity associated with the residual charge located between the gate and the 2deg and and a nd b represent the location of the charge as shown in Figure 11 (a). Figure 11 (b) plots the experimentally determined resonance positions against those theoretically obtained using Equation (15). In general, the conductivity, σ_o, of a semiconductor can be obtained from the doping and the mobility via

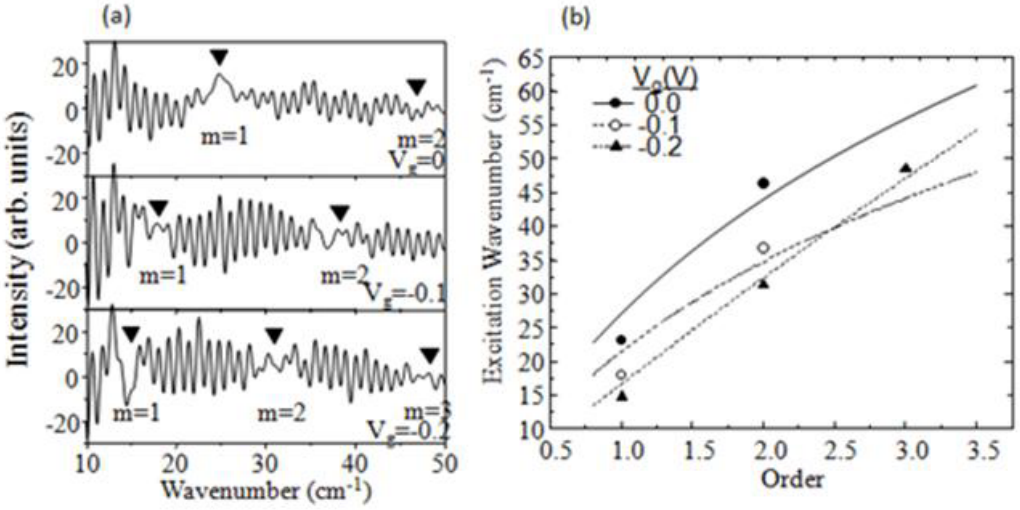

Figure 9: (a) Measured transmission through the HEMT of this work showing plasmon induced loss. (b) Comparison between experimentally and theoretically obtained plasmon resonance wavenumbers.

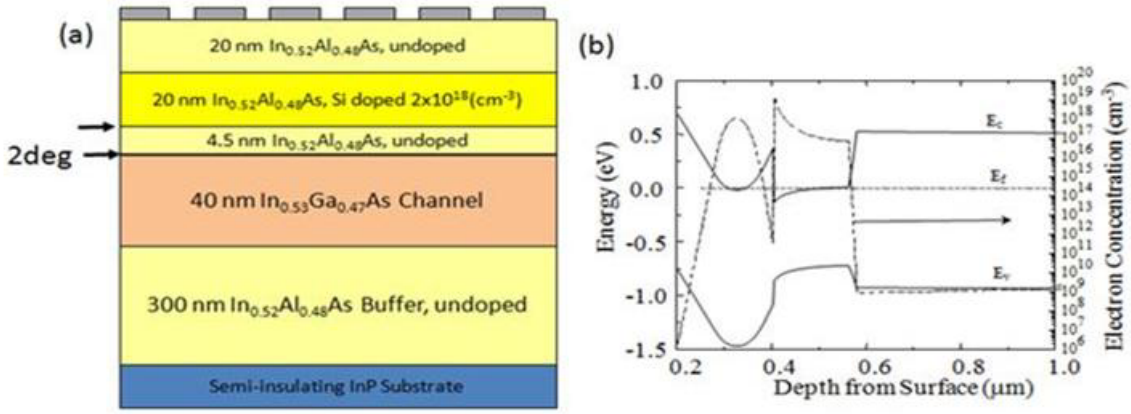

Figure 10: (a) Actual epilayer structure used in this work. (b) Calculated band diagram and charge concentration showing additional potential well and associated incomplete transfer of charge into the 2deg.

$$\sigma = qn\mu \tag{16}$$

where μ is, in this case, the electron mobility in the doped InAlAs layer. To obtain Figure 11 (b), n_s and σ_o were used as fitting parameters and were found to have values of roughly $3\text{x}10^{11}$ cm^{-2} and $4.5\text{x}10^{4}$ $1/\Omega\text{m}$ respectively. These values are consistent with the sheet charge density determined by other means and a the conductivity obtained from Equation (16) provided a mobility of 2000 cm^2/Vs and an InAlAs doping of $2.8\text{x}10^{18}$ cm^{-3} was used in the finite element simulation of Figure 10(b).

It has been shown that, due to fabrication constraints associated with plasmon coupling as well as the practical issue of maximum sheet charge concentration, the active plasmonic element described above is most suited for operation at THz frequencies. Although the response of this device was obtained by determining the FTIR transmission through the device, the overall usefulness of the device becomes greater if it is operated as a detector. It has been shown that changes in source to drain current of these plasmon mediated HEMTs accompanies the excitation of a plasmon mode. This effect is believed to be bolometric in nature and is the driving motivation behind this class of device where, because of its small foot print, the opportunity exists for frequency selective detection of THz radiation in an array format. The difficulty in optimizing such a device however, lies in the lack of narrow band, swept THz sources of sufficient power to reliably excite the device Figure 12 shows the time dependence of this device to high power pulses of THz radiation provided by the University of California Santa Barbara Free Electron Laser as a function of gate bias. Although a response is clearly seen coincident with the 12cm^{-1} excitation, the peak of this response is not seen to be altered by the gate bias suggesting a non-plasmon related effect. Pulse to pulse variations in laser power precluded the use of lock-in detection techniques to extract any usable plasmon related signal from the large background. The characterization of these devices operating as detectors and other active plasmonic based components is essential for their optimization and

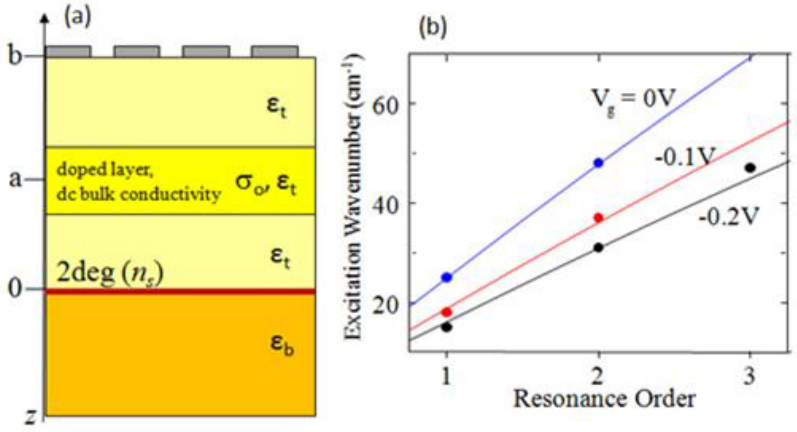

Figure 11: (a) Geometry of epilayer structure used in alternative dispersion relation of Equation (15) in the text. (b) Comparison between experiment and theory for allowed plasmon resonance as a function of order and gate bias using the alternate dispersion relation.

offers opportunities in the field of THz material characterization.

2.3 Integrated Quantum Optics

Quantum optics investigates the light/mater interaction at low photon densities where it has been found that classical electromagnetic theory fails. Quantum optic phenomenon such as photon entanglement, identical photons and photon blockade have no classical counterparts and have been used to motivate such applications as ultra secure communications, advanced imaging systems and quantum information science as well as exploring the fundamental limits defining classical and quantum physics. Historically, quantum optics research has been performed using bulk optical components due to the relative ease of producing entangled photons by way of non-linear crystals and spontaneous parametric down conversion. More recent work has focused on the technologically important short wave IR telecom wavelengths for the development of quantum repeaters and quantum key distribution systems. These applications offer the possibility of exploiting the photonic fiber infrastructure already in place but are hampered by the lack of single photon sources and single photon detectors at these wavelengths.

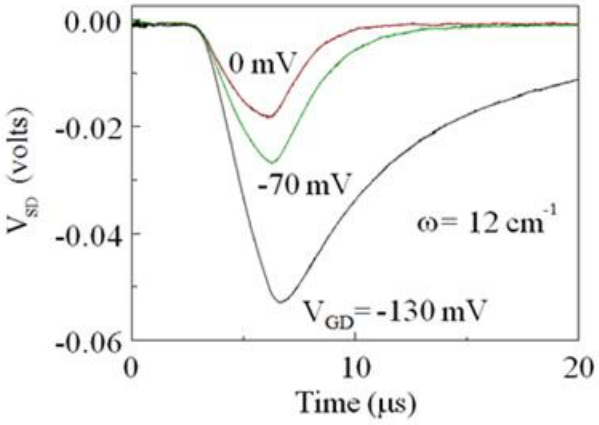

Figure 12: Source drain voltage as a function of time and gate bias when illuminated with pulses of 12cm^{-1} radiation. No shifts in resonance as a function of gate bias are observed.

To realize the full potential afforded by the quantum mechanical nature of the light/matter interaction, a number of groups are moving away from bulk optical components and investigating a completely integrated nanophotonic approach to quantum optic engineering [44-46]. The vision of having the single photon source, both active and passive optical components and an efficient single photon detector, integrated on a single semiconductor chip, with the ability to on demand, generate single photons, entangled photons and/or identical photons offers the possibility of high pixel count quantum imagers and mutli-qubit quantum co-processors while taking full advantage of the size and cost reduction afforded by the massive parallel processing capability of the present day semiconductor industry. At this stage, the choice of wavelength is secondary to the ability to integrate all components on chip. Should off chip light sources be required, or, the transmission of information down an optical fiber be desired, non-linear parametric processes can be used for wavelength conversion. Ultimately however, a fully integrated approach for a quantum optics based chip, performing a specific quantum optics based function, such as a quantum computation, could be achieved with electrical signals as both the input and the output. In this case, that wavelength which facilitates the quantum based functionality is the most appropriate wavelength irrespective of the availability of the bulk optic components required for similar functionality on an optical table. To be clear, the suggestion here is that simply because a bulk optical component exists, such as a single photon source or a single photon detector, which operates at a specific wavelength, this in and of itself should not make this the a-priori wavelength of choice when investigating chip scale integrated quantum optics. In fact, there are numerous reasons, as will be discussed below, why longer wavelengths might be preferable for integrated quantum optics, offering new opportunities in both material characterization and component development at THz frequencies.

Essential for the realization of a number of quantum optics based applications is the ability to couple atomic states to cavity modes. When considering integrated quantum optics, the role of atomic states is taken by, for example, by the photon mediated electronic transitions of a quantum dot. This atomic-like system is fabricated inside a suitable cavity such as Fabry-Perot cavity or a photonic crystal cavity. Depending on the application, the system needs to be placed in either the so-called “strong” or “weak” coupling regimes. Strong and weak coupling can be understood by considering the energies associated with such a coupled atomic-like/cavity system given by

$$E_{+,-} = \Delta E - \frac{i(\gamma+\kappa)}{4} \pm \sqrt{g^2 - \frac{(\kappa-\gamma)^2}{16}} \tag{17}$$

where ΔE is the ground to excited state transition of the atomic-like state, γ and κ are the electronic transition and cavity de-phasing rates respectively and g is the coupling constant associated with the atomic-like state and the cavity. In general, g is given by

$$g = \sqrt{\frac{\mu^2 E_c}{n^2 2\varepsilon_o V}} \tag{18}$$

with μ being the dipole moment associated with the electronic transition, n is the index of refraction of the non-resonant semiconductor material, E_c and V are the eigen-energies of the bare cavity and the volume of the cavity respectively. In this case, assuming no detuning between the cavity and the transition, $E_c = \Delta E$. Considering equation (17), if $g^2 \leq (\gamma - \kappa)^2/16$ the system is in the so called "weak coupling regime" and the real parts of $E_{+,-}$ will be degenerate. In this case, enhancement of the atomic-like states spontaneous emission rate will be observed as a broadening of the spectral line shape. If, however, $g^2 > (\gamma - \kappa)^2/16$ the system is in the so called "strong coupling regime" and $E_{+,-}$ takes on two distinct values and is observed as a splitting of the spectral line shape into two distinct peaks. This so called vacuum Rabi splitting, VRS, is the result of energy oscillating between the cavity mode and the electronic transition associated with the atomic-like state. Figure 13 (a) plots Equation (17) as a function of the coupling strength g and clearly shows the two coupling regimes while Figure 13 (b) shows experimental results illustrating VRS for a quantum dot system in a photonic crystal cavity.

If required for a particular application, strong coupling can be achieved by utilizing systems with a stronger dipole moment or using cavities with small volumes as seen by considering Equation (18). Because, in semiconductor systems, extremely strong dipole moments are associated with the inter-sub-band transitions of quantum wells, QW's, such systems serve as the motivation for mid-IR spectroscopy to aid the development of integrated quantum optic chips [46-48]. Although this quantum well/cavity system has been used to successfully demonstrate strong coupling, they are inherently a two dimensionally confined system and as such do not, in general, lend themselves to operating in the desired single photon regime. For single photon applications, three dimensional confinement is needed, hence the interest in quantum dots, QD's. QD's have the required three dimensional confinement but at the cost of a weaker dipole moment due to their reliance, in general, on valence to conduction band transitions. In addition, although much research is being turned to this problem, there is difficulty in determining the precise location where a single QD will form and as such, placing the QD at the correct location in a cavity is problematic. To solve this problem some groups are investigating, through lateral etching and epilayer regrowth, the possibility of turning a quantum well system into a QD

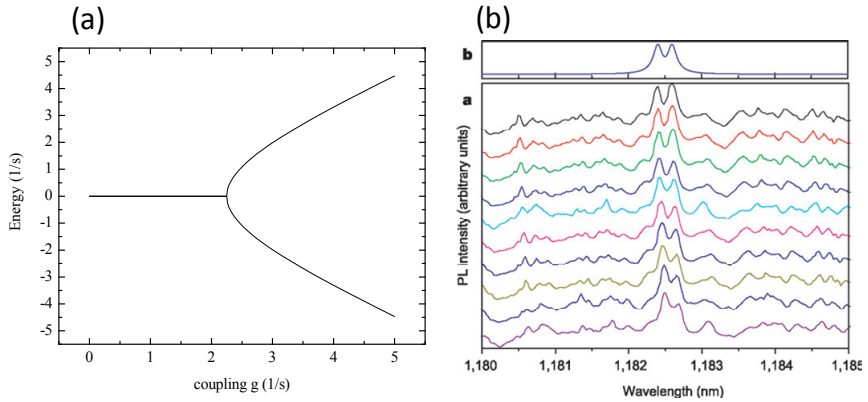

Figure 13: (a) Energy splitting of first excited state of an atomic transition as a function of atom/cavity mode coupling showing "weak" and "strong" coupling regimes. (b) Photoluminescence data showing Vacuum Rabi splitting associated with a quantum dot in a photonic crystal cavity (from Ref. (45))

system. Using such a method the inter-sub-band-transitions and their stronger dipole moments become accessible as well as the ability to precisely from the dot at any desired location, however, due to geometrical consideration, the inter-sub-band-transition energies associated with these etched structures shifts to longer wavelengths and THz frequencies [49,50].

The deterministic placement of dot location obtained by converting a quantum well into a quantum dot, as well as the stronger dipole moment, is not the only motivation to investigate integrated quantum optics at longer wavelengths. As stated above, reducing the cavity volume will also allow for an increase in the coupling strength which will allow easier access to the strong coupling regime. To exploit this property, a number of groups are investigating the coupling of the cavity modes associated with metallic, plasmon based, nano-cavities to quantum dot transitions [51]. In this regard, longer wavelengths are preferred for all of the same reasons mentioned in the previous sections of this work, namely, larger geometries ease fabrication constraints and longer wavelengths are inherently less lossy. In addition, the increased mode height associated with a plasmonic cavity at longer wavelengths allows the quantum structure to be further from the surface minimizing the effect of surface states on the QD transition rates.

The final motivation for investigating integrated quantum optics at THz frequencies is related to the availability of on-chip light sources. At present, motivated by the telecom industry, there is a tremendous push to drive costs down by moving to Si based photonics. Although wave guiding structures and a variety of Si photonic components are being developed, a monolithically integrated on-chip light source remains elusive. Present schemes for chip excitation are direct bonding of III-V lasers to patterned Si. Although a workable solution, by moving to longer wavelengths the possibility of integrating a quantum cascade laser, QCL, with the underlying integrated quantum optic matrix is a distinct possibility. QCL's, as a uni-polar device, do not rely on band to band transitions for the photon generation process and therefore are inherently transparent at the emitting wavelength. This leads to the possibility of the waveguide being formed from the same epi-layer structure as the QCL itself, minus the current injection used to begin the cascade process [52].

Although the development of an integrated nanophotonic quantum optic chip, with an integrated light source, quantum interaction region and integrated detector would be the final goal, the development of such a chip will require THz spectroscopy to be performed initially on nanophotonic components. This will require launching of long wavelength radiation into micron size waveguides. This motivates the development of new, high brightness, micro-spectroscopic techniques at the long wavelengths. One such method is THz comb-FTIR, which is discussed below.

2. THz COMB-FTIR

The THz spectroscopic investigations of metamaterials, active plasmonic components and integrated quantum optics components seems warranted based on metamaterial fabrication constraints, plasmonic loss, the large dipole moments associated with quantum well inter-sub-band transitions, the potential for ultra small plasmonic cavities and the possibility of fully integrated light sources using long wave QCL's. All of these applications require the ability to acquire spectroscopic information from components that are millimeters in size. In the case of integrated quantum optics, this problem is further compounded when the micron size of typical THz plasmonic, dielectric or hybrid waveguides are considered. Although many THz spectroscopic techniques are available, the overall research effort would benefit, and in the case of integrated quantum optics at long wavelengths become possible, if higher brightness sources and associated techniques were developed for characterizing these low, signal-to-noise ratio components. One such technique actively being pursued by a number of groups is comb-FTIR, or, c-FTIR. Initially developed at THz frequencies and improved for use at wavelengths from 7μm to 12μm, the use of this high brightness, coherent detection technique at the original THz frequencies offers challenges as well as opportunities to expand the field of THz spectroscopy into those areas described above [18,19].

C-FTIR is a multi frequency heterodyne detection technique that utilizes the frequency comb generated by, for example, a mode locked Ti/Sapphire, Ti/S, laser [53]. The cavity of a Ti/S laser has a mode structure shown schematically in Figure 14 (a). In the frequency domain, it is composed of equally spaced frequencies, with the separation of the frequencies, f_{rep}, determined by the inverse of the time it takes light to transverse the cavity. Also in the figure is shown the frequency range associated with the gain medium of the oscillator and is seen to span a number of these allowed modes. For a laser to operate in continuous wave, CW, mode all but one of the modes located under the gain curve is allowed to oscillate and the output can be represented by a single frequency. If, through the use of a saturable absorber

for example, the energy coupling to any one particular mode can be limited and the overall energy of the system is forced to be shared among all modes under the gain curve. In this case, the output can be represented as a sum of multiple discrete frequencies, which, when Fourier transformed into the time domain, no longer looks like a continuous wave but takes on the characteristics of a very short, intense pulse of laser light, emitted at the f_{rep} frequency. In general, the modal structure of this cavity is not harmonic in that the frequency "comb" cannot be represented as an integer multiple of a single, fundamental frequency. Differences between the phase and group velocity of the individual modes and the overall output pulse cause a shift in the comb frequencies called the carrier offset envelope, *COE*. In general, therefore, any one particular frequency associated with the comb, f_o, can be written as

$$f_o = m_o f_{rep} + COE \tag{19}$$

where m_o is an integer. However, if this comb is incident on an appropriate non-linear element, difference frequency generation occurring between frequencies will produce a new, harmonic comb, as the constant *COE* value is subtracted during the non-linear mixing process. This harmonic curve will also provide photons at only those frequencies that had satisfied the phase matching conditions associated with the type of non-linear element used.

C-FTIR utilizes two such harmonic combs detuned with regards to repetition rate by a beat frequency, f_b, given simply as

$$f_b = \left| f_{rep1} - f_{rep2} \right| \tag{20}$$

where f_{rep1} and f_{rep2} are the repetition rates of the first and second oscillators respectively[18,19]. When both beams are passed through the same non-linear element, at a rate given by the beat frequency, the short pulses, and in-turn the different frequency combs, will be precisely aligned in both time and space and produce a so-called harmonic "dual-beam" as shown in Figure 14 (c). If this dual-beam is incident on a detector that has the appropriate spectral and electronic bandwidth, an interferogram will result which, when Fourier transformed, will produce the spectral content of the original dual beam, but scaled down in frequency by a factor *S* given by

$$S = \frac{f_{rep}}{f_b} \tag{21}$$

To illustrate this concept, consider two Ti/S oscillators, one with f_{rep}=124MHz and the other detuned by f_b=100Hz, illuminating a Ga/Se crystal to produce a dual beam centered at a 10μm wavelength or a frequency of $3\text{x}10^{13}$Hz. This optical frequency is far too fast to detect directly, but, after scaling by the factor *S* of Equation (21) is down converted to a measurable RF frequency of 24MHz. Figure 15 shows the results of this technique used to detect trace Acetone vapors

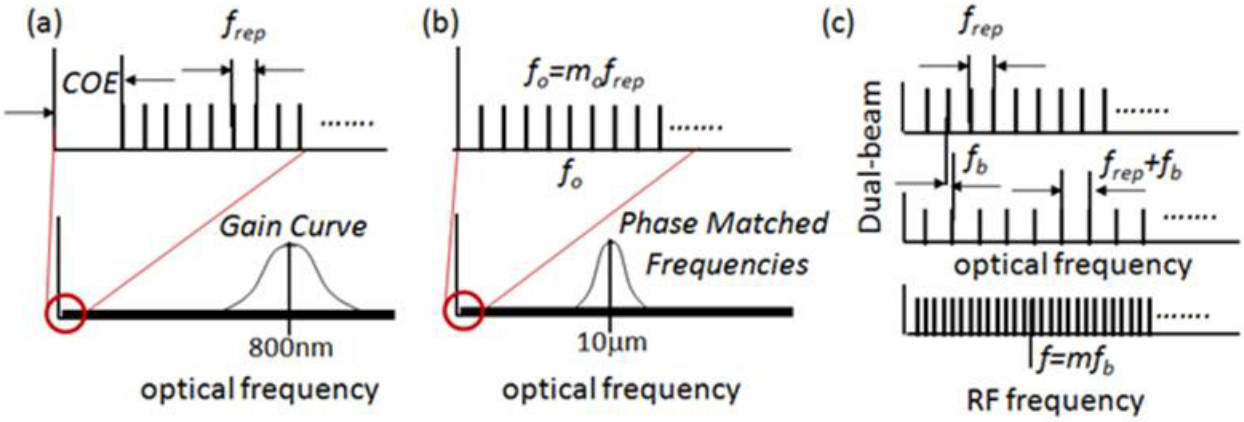

Figure 14: (a) Frequency comb associated with a typical mode-locked Ti/S oscillator showing comb spacing and gain curve. (b) Harmonic frequency comb obtained using difference frequency generation via a GaSe non-linear crystal. (c) Dual beam obtained using two, detuned Ti/S oscillators illustrating scaling from optical to RF frequencies using the c-FTIR technique.

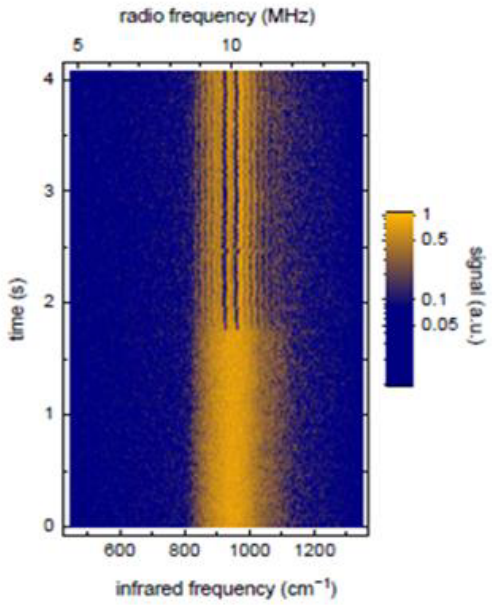

Figure 15: Experimental data of Acetone vapor spectrum obtained using c-FTIR technique at a distance of 43m. Vapor was introduced at roughly 1.75sec. From Ref. (18)

remotely at a distance of 43m and illustrates the power of this high brightness, coherent detection technique.

Beyond the engineering complexities of two mode-locked lasers operating at a 10Hz difference frequency, the spectral bandwidth accessible using this technique is determined by the non-linear element used to create the dual beam, and the detector used to generate the interferogram. For the illustration discussed above, a Ga/Se crystal will produce the dual beam and an MCT detector with 50MHz electronic bandwidth is suitable and readily available. For THz applications, bulk photoconductive switches can be used as a source radiating from 0.3 THz to 3THz. This will require a detector with a similar spectral bandwidth but with an electronic response from roughly 200kHz to 3MHz if the previously derived scaling factor of 1.24×10^6 is used. Typical detectors with this spectral response, such as Si bolometers, are too slow to respond even at the scaled down frequencies [54]. Niobium Nitride, NbN, hot electron bolometers offer the high speed response but suffer at the lower THz frequencies and require cooling to below 4K [55]. One promising approach is to use recently available quasi-optic, zero bias, Schottky diode detectors. These detectors offer room temperature performance over the necessary bandwidth. Although not as sensitive as bolometers, the high brightness and coherent detection scheme offered by the c-FTIR technique might make them suitable [56].

3. CONCLUSION

A number of non-traditional research efforts utilizing THz frequencies have been proposed. Metamaterial investigations at THz frequencies ease fabrication constraints and offer a means to compare theory to experiment with relatively low loss. The control of plasmonics modes due to charge density changes requires THz frequencies based on plasmon coupling constraints and the overall charge densities presently available in the semiconductor systems used to confine the charge. THz based integrated quantum optic research offers easier access to the strong coupling regime, the potential for the deterministic placement of quantum dots as well as the possibility of a chip scale format. Finally, c-FTIR performed using bulk photoconductive switches and quasi-optic Schottky diode detectors are presented as a means to perform THz spectroscopy on these micro-systems. It is hoped that these ideas will foster, at the very least, a brief re-examination of research interests and a determination if benefits could be gained by performing that research at what might be considered a “non-traditional” frequency.

4. ACHNOWLEDGEMENTS

The author would like to acknowledge the Air Force Office of Scientific Research, LRIR awards 09RY09COR and 09RY08CORCOR, Dr. Gernot Pomrenke, program manager, for funding this work as well as Dr. Joshua Hendrickson of the Air Force Research Laboratory, Hanscom AFB, for a critical reading of portions of this manuscript.

REFERENCES

[1] Hebling, K Yeh, M.C. Hoffmann, and K. A. Nelson *“High-Power THz Generation, THz Nonlinear Optics and THz Nonlinear Spectroscopy”* IEEE Journal of Selected Topics in Quantum Electronics, **14**, 345, (2008)

[2] J.F. O’Hara, A. J. Taylor, H. Chen, W. J. Padilla, R. D. Averitt, A. C. Gossard, C. Highstrete and M. Lee, “*Electromagnetic Metamaterials for Terahertz Applications”* , Terahertz Science and Technology, **1**, 42, (2008)

[3] J. Gu, R. Singh, Z. Tian, W. Cao, Q. Xing, M. He, J.W. Zhang, J. Han, H. Chen and W. Zhang, *“Terahertz superconductor metamaterial”,* Applied Physics Letters **97**, 071102 (2010)

[4] M. Dragoman, D. Dragoman, *"Plasmonics: Applications to nanoscale terahertz and optical devices"*, Progress in Quantum Electronics, **32**, 1 (2008)
[5] M. Yu, M. Huang, D.E.Savage, M.G. Lagally, R.H. Blick *"Local-wetting-induced deformation of rolled-up Si/Si-Ge nanomembranes: A potential route for Remote chemical sensing"* IEEE transactions on Nanotechnology, **10**, 21 (2011)
[6] R. Piesiewicz, T. Kleine-Ostmann, N. Krumbholz, D. Mittleman, M. Koch, J. Schoebel and T. Kurner *"Short-range ultra-broadband terahertz communications: concepts and perspectives"* IEEE Antenna and Propogation magazine, 49, 24 (2007)
[7] P. Siegal, *"THz instruments for space" IEEE Transactions on Antennas and propogation",* **55,** 2957 (2007)
[8] K.B. Cooper, R.J. Dengler, N. Llombart, T. Bryllert, G. Chattopadhyay, E. Schlecht, J. Gill, C. Lee, A. Skalare, I. Mehdi and P.H. Siegal *"Penetrating 3-D imaging at 4- and 25-m range using submillimeter-wave radar"* IEEE Transactions on Microwave Theory and Techniques, **56**, 2771 (2008)
[9] M. Tonoughi, *"Cutting edge terahertz technology"* , Nature Photonics, **1**, 97 (2007)
[10] E. Mueller, A. DeMaria*,"Broad bandwidth communication/data links using terahertz sources and Schottky diode modulators/detectors"* Proc. SPIE, 5727, 151 (2005)
[11] S. Fiorino, P. Grice, M. Krizo, R. Bartell, J. Haiducek and S. Cusumano *"Lab measurements to support modeling terahertz propagation in brownout conditions"* Proc. SPIE, 7671, 76710W (2010)
[12] J. liu, J. Dai, S. Chin and X.-C. Zhang, *"Broadband terahertz wave remote sensing using coherent manipulation of fluorescence from asymmetrically ionized gases"* Nature Photonics, **4**, 627 (2010)
[13] J.F. Federici, B. Schulkin, F. huang, D. Gary, R. Barat, F. Oliveira and D. Zimdars *"THz imaging and sensing for security applications_explosives, weapons and drugs"* Semicond. Sci. Technol, **20**, S266 (2005)
[14] M. Fitch, R. Osiander, *"Terahertz waves for communications and sensing"* Johns Hopkins APL Technical Digest, **25**, 348 (2004)
[15] H.Tao, A. Strkwerda, M. Liu, J. Mondia, E. Ekmekci, K. Fan, D. Kaplan, W. Padilla, X. Zhang, R. Averitt and F. Omenetto *"Performance enhancement of terahertz metamaterials on ultrathin substrates for sensing applications"* Applied Physics letters **97**, 261909 (2010)
[16] J. Kim, R. Soref and W. R. Buchwald *"Multi-peak electromagnetically induced transparency (EIT)-like transmission from bull's-eye-shaped metamaterial"* Optics Express, **18**, 17997 (2010)
[17] M. Sherwin, A. Imamoglu and T. Montroy *"Quantum computation with quantum dots and terahertz cavity quantum electrodynamics"* Phys. Rev. A, **60**, 3508 (1999)
[18] D. van der Weide, J. Murakowski and F. Keilman *"Gas-absorption spectroscopy with electronic terahertz techniques"* IEEE Transactions on Microwave theory and Techniques, **48**, 740 (2000)
[19] A. Schliesser, M. Brehm, F. Keilmann and D. van der Weise *"Frequency-comb infrared spectrometer for rapid, remote chemical sensing"* Optics Express, **13**, 9029 (2005)
[20] H. Saxena, R. E. Peale and W.R. Buchwald *"Tunable two-dimensional plasmon resonances in an InGaAs/InP HEMT"*, Journal of Applied Physics, **105**, 113101 (2009)
[21] X. Xiao,J. Wu, F. Miyamaru, M. Zhang, S. Li, M. W. Takedo, W. Wen and P. Sheng *"Fano effect of metamaterials resonance in terahertz extrodinary transmission"*, Applied Physiecs Letters **98**, 011911 (2011)
[22] G. Medhi, A.V. Muravjov, H. Saxena, J.W. Cleary, C.J. Frerickson, R.E. Pelae and O. *Edwards "Infrared intracavity laser absorption spectrometer"* Proc. SPIE, 7680, 76800N (2010)
[23] J.B. Pendry, A.J. Holden, W.J. Stewart and I. Youngs *"Extremely low frequency plasmons in metallic mesostructures"* Physical Review Letters, **76**, 4773 (1996)
[24] J.B. Pendry, A.J. Holded D.J. Robbins and W.J. Stewart *"Magnetism from conductors and enhanced nonlinear phenomenon"* IEEE Transactions on Microwave Theory and Techniques, **47**, 2075 (1999)
[25] T. Koschny, M. Kafesaki, E.N. Economou and C.M. Soukoulios *"Effective medium theory of left-handed materials"* Physical Review Letters, **93**, 107402 (2004)
[26] C.G. Parazzoli, R.B. Greegor, K. Li, B.E.C. Koltenbah and M. Tanielian *"Experimental verification and simulation of negative index of refraction using Snell's law"* Physical Review Letters, **90**, 107401 (2003)
[27] Z.-G. Dong, M.-X. Xu, S.-Y. Lei, H. Liu, F.-M. Wang and S.-N. Zhu *"Negative refraction with magnetic resonance in a metallic doublr-ring metamaterials"* Applied Physics Letters, **92**, 064101 (2008)
[28] Z.-G. Dong, M.X. Xu, H. Lui and S.-N. Zhu *"Parametric simulations of the metallic double-ring metamaterials: Geometric optimization and terahertz response"* Journal of Applied Physics, **105**, 034907 (2009)
[29] J. B. Pendry,D. R. Smith *"ReversinglLight: Negative refraction"* Physics Today, December (2003)

[30] V.G. Veselago, *"The electrodynamics of substances with simultaneously negative values of both ε and μ"* Soviet Physics USPEKHI, **10**, 509 (1968)
[31] S. Linden, C. Enkrich, M. Wegener, J. Zhou, T. Koschny and C.M. Soukoulis *"Magnetic response of metamaterials as 100 terahertz"* Science, **306**, 1351 (2004)
[32] J.W. Cleary, R.E. Peale, D. J. Shelton, G.D. Boreman, C.W. Smith, M. Ishigami, R. Soref, A. Drehman and W.R. Buchwald, *"IR permittivities for silicides and doped silicon",* J. Opt. Soc. Am. B, **27**, 730 (2010)
[33] M. L. Brongersma, P. G. Kik "*Surface Plasmon Nanophotonics"* (Springer, 2007)
[34] S. A. Maier, "*Plasmonics: Fundamentals and Applications"* (Springer, 2007).
[35] S.A. Maier, P.E. Barclay, T.J. Johnson, M.D. Friedman and O. Painter *"Low-loss fiber accessible plasmon waveguide for planar energy guiding and sensing"* Applied Physics Letters, **84**, 3990 (2004)
[36] X, Zhang and Z. Liu *"Superlenses to overcome the diffraction limit"* Nature Materials, **7**, 435 (2008)
[37] H. Raether, *"Surface Plasmons on Smooth and Rough Surfaces"* (Springer, 1986).
[38] J.W. Cleary, G. Medhi, R.E. Peale and W.R. Buchwald *"Long-wave infrared surface plasmon grating coupler"*, Applied Optics, 49, 3102 (2010)
[39] A. Hessel, A. A. Oliner, *"A new theory of Wood's anomalies on optical gratings,"* Appllied Optics, **4**, 1275 (1965).
[40] R.W. Wood, *"On a remarkable case of uneven distribution of light in a diffraction grating spectrum",* Philos. Mag., **4**, 396 (1902)
[41] S.J. Allen, D.C. Tsui and R.A. Logan *"Observation of 2-dimensional plasmon in silicon inversion layers"* Physical Review Letters, **38**, 980 (1977)
[42] X.G. Peralta, S.J. Allen, M.C. Wenke, N.E. Harff, J.A. Simmons, M/P/ Lilly, J..L. Reno, P.J. Burke and J.P. Eisenstein *"Terahertz photoconductivity and plasmon modes in double-quantum-well field-effect transistors"* Applied Physics Letters, **81**,1627 (2002)
[43] Greg Azin, Private communication, City University of New York, Kingsborough NY
[44] G. Khitrova, H.M. Gibbs, M. Kira, S.W. Koch and A. Scherer "*Vacuum Rabi splitting in semiconductors"* Nature Physics, **2**, 81 (2006)
[45] T. Yoshie, A. Scherer, J. Hendrickson, G. Khitrova, H.M. Gibbs, G. Rupper, C. Ell, O.B. Shchekin and D.G. Deppe *"Vacuum Rabi splitting with a single quantum dot in a photonic crystal nanocavity",* Nature, **432**, 200 (2004)
[46] J.P. Retihmaier, G. Sek, A. Loffler, C. Hofmann, S. Kuhn, S. Reitzenstein, L.V. Keldysh, V.D. Kulakovskli, T.L. Reinecke and A. Forchel *"Strong coupling in a single quantum dot-semiconductor microcavity system"* Nature, **432**, 197 (2004)
[47] C. Ciuti, I. Carusotto *"On the ultrastrong vacuum Rabi coupling of an intersubband transition in a semiconductor microcavity"* Journal of Applied Physics, **101**, 081709 (2007)
[48] E. Dupont, J.A. Gupta and H.C. Liu *"Giant vacuum-field Rabi splitting of intersubband transitions in multiple quantum wells"* Physical Review B, **75**, 205325 (2007)
[49] D. Dini, R. Kohler, A. Tredicucci, G. Biasiol and L. Sorba *"Microcavity polariton splitting of intersubband transitions"* Physical Review Letters, **90**, 116401 (2003)
[50] L. Claudio, A. Panzarini, G. Panzarini, J.-M. Gerard, *"Strong-coupling regime for quantum boxes in pillar microcavities: Theory"* Physical Review B, **60**, 276 (1999)
[51] N. Meinzer, M. Rither, S. Linden, C.M. Soukoulis, G. Khitrova, J. Hendrickson. J.D. Olitzky, H.M. Gibbs and M. Wegener *"Arrays of Ag split-ring resonators coupled to InGaAs single-quantum-well gain"* Optics Express, **18**, 24140 (2010)
[52] B.G. Lee, M.A. Belkin, R. Audet, J. MacArthur, L. Diehl, C. Pflugl, F. Capasso, D. Oakley, D. Chapman, A. Napoleone, D. Bour, S. Corzine, G. Hofler and J. Faist, *"Widely tunable single-mode quantum cascade laser source for mid-infrared spectroscopy"* Applied Physics Letters, **91**,231101 (2007)
[53] S.T. Cundiff , J. Ye *"Colloquium: Femtosecond optical frequency combs"* Reviews of Modern Physics, **75**, 325 (2003)
[54] T. Yasui, Y. Kabetani, E. Saneyoshi, S. Yokoyama and T. Araki *"Terahertz frequency comb by multi-frequencyp heterodyning photoconductive detection for high-accuracy, high-resolution terahertz spectroscopy"* Applied Physics Letters, **88**, 241104 (2006)
[55] F. Rodriguez-Morales, K.S. Yngvesson and D. Gu *"Wideband IF-integrated Terahertz HEB Mixers: Modeling and characterization"* IEEE Transactions on Microwave Theory and Techniques,**58**, 1140 (2010)
[56] L. Liu, J.L. Hesler, H. Xu, A.W. Lichtenberger and R.M. Weiklell *"A broadband quasi-optical terahertz detector utilizing a zero bias schottky diode"* IEEE Microwave and Wireless Components Letter, **20**, 505 (2010)